



TAYLOR SIMULATION AND EXPERIMENTAL INVESTIGATION OF ROLLING TEXTURES OF POLYCRYSTALLINE IRON ALUMINIDES WITH SPECIAL REGARD TO SLIP ON $\{112\}$ PLANES

D. RAABE

Institut für Metallkunde und Metallphysik, RWTH Aachen, Kopernikusstr. 14, 52056 Aachen, Germany

(Received 17 January 1995; in revised form 31 May 1995)

Abstract—The evolution of the crystallographic rolling textures of B2- and DO₃-ordered polycrystalline iron aluminides is described in terms of Taylor-type simulations. The contribution of crystallographic slip on the various types of glide systems, particularly the influence of $\{112\}\langle 111 \rangle$ slip is examined. The evolution of the aspect ratio of the grains during rolling is considered by gradually relaxing the externally imposed strain constraints with increasing deformation. For simulating low reductions, full constraints Taylor-type conditions are assumed. For describing intermediate reductions the lath model and for large reductions the pancake model is employed. The ratio of the critical resolved shear stress of the $\{110\}\langle 111 \rangle$ and $\{112\}\langle 111 \rangle$ slip systems is varied. The predictions yielded by impeding $\{110\}\langle 111 \rangle$ systems and promoting $\{112\}\langle 111 \rangle$ systems ($\tau_{\{110\}\langle 111 \rangle} = 10 \times \tau_{\{112\}\langle 111 \rangle}$) are in good accord with experiment. The results are discussed in terms of the energy of the antiphase boundaries and of dislocation core effects.

Zusammenfassung—Die Entwicklung der kristallographischen Walztexturen von B2 und DO₃ geordneten Eisen-Aluminiden wird mit Hilfe von Taylorsimulationen beschrieben. Der Beitrag der kristallographischen Gleitung auf den verschiedenen Typen von Gleitsystemen, insbesondere der Einfluß der $\{112\}\langle 111 \rangle$ Gleitsysteme wird untersucht. Die Entwicklung der Kornform während des Walzens wird durch eine zunehmende Relaxation der von außen vorgegebenen Verformungsbeschränkungen im Verlauf zunehmender Verformung berücksichtigt. Für die Simulation geringer Umformgrade wird vollständige Verformungskompatibilität im Sinne des 'Full Constraints' Taylor Modells angenommen. Zur Beschreibung mittlerer Umformgrade wird das sogenannte 'Lath' Modell und für hohe Umformgrade das sogenannte 'Pancake' Taylor Modell angewendet. Das Verhältnis der kritischen Schubspannung auf den $\{110\}\langle 111 \rangle$ und $\{112\}\langle 111 \rangle$ Gleitsystemen wird variiert. Die Modellvorhersagen, bei denen die Gleitung auf $\{110\}\langle 111 \rangle$ Systemen behindert und auf $\{112\}\langle 111 \rangle$ Systemen begünstigt wird ($\tau_{\{110\}\langle 111 \rangle} = 10 \times \tau_{\{112\}\langle 111 \rangle}$) weisen eine gute Übereinstimmung mit den experimentellen Beobachtungen auf. Die Ergebnisse werden auf der Basis von Versetzungskerneffekten und der Energie der Antiphasengrenzen erörtert.

1. INTRODUCTION

The mechanical properties as well as the excellent oxidation and sulfidation resistance of intermetallic iron aluminides with compositions near that of FeAl (B2) and Fe₃Al (B2 or DO₃) at low and elevated temperatures have long stimulated the research in this field [1–17]. The DO₃ unit cell consists of four interpenetrating face centred cubic (f.c.c.) sublattices, one of which for the state of perfect order is occupied entirely by aluminium atoms. For perfect B2-type long-range order, two of the sublattices are occupied by aluminium atoms.

Especially, imperfectly B2 ordered Fe₃Al based alloys are promising in industrial terms, e.g. Refs [13, 14]. The production of such Kurnakov-type compounds requires relatively small material costs. Furthermore, these alloys [11, 13, 14] reveal a better strength-to-weight ratio than some stainless steels.

Due to the control of microstructure and composition, the corrosion resistance and the mechanical properties of Fe₃Al-based alloys were considerably improved, especially the room temperature ductility and the strength at elevated temperatures [11–14]. Numerous studies have tackled the influence of ternary additions like Cr, Mo, Zr, Nb, Hf, C and B on the properties of these compounds [11–14]. Most of the alloys presently under investigation reveal a B2-type structure with perfect (FeAl) or imperfect (FeAl and Fe₃Al containing up to 7 alloying elements) long-range order. Pure iron aluminides with more than 24 at % aluminium content usually reveal a DO₃-type long-range order after slow cooling of only 10–20 K/day [8, 9, 11, 12, 18–20]. However, in the case of rapid cooling or thermomechanical treatment of iron aluminides with ternary additions, extensive primary solid solutions have been observed which include long-range ordered areas based

upon both the B2 and DO₃ structures, e.g. Refs [4, 8, 11–14].

For clarifying the underlying mechanisms of the strength and ductility of plastically deformed Fe₃Al-based and comparable B2- or DO₃-type alloys essentially two methods were employed in the past. First, the influence of the antiphase boundary (APB) energy was assessed on the selection of slip systems [5–12, 21–26]. Second, slip trace investigation on polished sample surfaces as well as transmission electron microscopy were employed [4–12, 21–25, 27–30]. In long-range ordered crystals, superlattice rather than ordinary lattice dislocations are the carriers of plastic deformation, e.g. Refs [11, 17]. The motion of imperfect superlattice dislocations gives rise to the generation of antiphase boundaries. In B2-ordered alloys two-fold dissociated and in DO₃ ordered alloys (Fe₃Al and Fe₃Si) two- and four-fold dissociated superlattice dislocation configurations were observed [11, 17, 31, 32]. Such dislocations are generated only when the magnitude of the externally imposed stress suffices to allow for production of the APB, e.g. Refs [7–11, 17, 21]. The presence of APB implies that superlattice dislocations cannot easily change their actual glide planes. It was shown that both the type of slip systems and the types of superlattice dislocations involved are determined by composition, temperature, strain rate and heat treatment prior to deformation, e.g. Refs [11, 17]. Consequently, these parameters revealed a considerable influence on the appearance of the slip line traces on polished sample surfaces (wavy or straight) [8, 9, 22–28]. The two types of slip line markings were usually interpreted in terms of deformation via ordinary (wavy) or superlattice (straight) dislocations. Concerning the active slip systems, it was shown that dislocation movement in perfectly or imperfectly B2- and DO₃-ordered alloys at elevated temperatures essentially takes place on those glide systems, which are typically activated in non-ordered body centred cubic (b.c.c.) alloys [11, 17]. Whereas the occurrence of {110}⟨111⟩ slip systems seems to be promoted by their low APB energy, the strong tendency for {112}⟨111⟩ slip especially at low temperatures probably stems from dislocation core effects [15–17, 29]. Additionally, the activation of glide systems with a ⟨100⟩ Burgers vector and {001} or {011} slip planes was predicted [11, 15–17, 22, 23, 30]. Albeit numerous, details of plasticity of iron aluminides were clarified by use of the techniques cited above, a quantitative assessment of the contribution of the various types of slip systems to large strain deformation was not yet achieved. Excellent reviews on this subject were recently submitted by McKamey *et al.* [11] and Umakoshi [17].

For the examination of plasticity of iron aluminides, especially at large strains, the employment of quantitative texture analysis [33, 34] seems to be a beneficial additional diagnostic tool for two reasons. Firstly, the evolution of the crystallographic texture

during plastic deformation is directly connected with the displacement gradient tensor which results from the shear imposed by the active slip systems [35]. This close geometrical relationship between crystallographic slip on the one hand and the resulting grain orientations on the other hand enables one to employ textures as a probe for the determination of the slip systems which contribute to plastic deformation [35–37]. Secondly, the directional behaviour of polycrystals is generally an integral property of their orientation distribution. Fe₃Al based alloys with up to 5 mass% Cr content are considered as potential candidates for applications where ferritic stainless steels with about 17 mass% Cr are nowadays in use, e.g. Refs [11, 13, 14]. Consequently, their directional plastic properties, especially their deep drawing behaviour, should be studied. The first investigations about the crystallographic textures of deformed and heat-treated polycrystalline iron aluminides and comparable B2-ordered alloys were recently submitted by Mao and Sun [38, 39] and Raabe [40–42].

In the present study, the crystallographic textures which are developed during rolling of polycrystalline intermetallic FeAl- and Fe₃Al-based B2- and DO₃-ordered or partially-ordered aggregates are simulated by means of Taylor-type models. Special attention is drawn to the gradual relaxation of the externally imposed strain constraints with increasing deformation and to the critical resolved shear stress (CRSS) of the {110}⟨111⟩ and the {112}⟨111⟩ slip systems. The predicted orientation distributions are compared to experimental results.

2. SIMULATION METHOD

In the present study, the rolling textures of perfectly- and imperfectly-ordered iron aluminides are simulated by means of a Taylor-type model. Texture simulations according to Taylor [35] are based on the description of macroscopic deformation by means of crystallographic slip. The macroscopic deformation is characterised by the so-called distortion or displacement gradient tensor written in lattice coordinates. Its symmetric part represents the strain tensor, while the antisymmetric part describes the resulting plastic rigid body rotation (not the grain rotation). From the latter tensor and the displacement gradient tensor written in machine coordinates the relevant orientation changes, i.e. the lattice rotations can be calculated, e.g. Refs [43–45].

The macroscopic deformation during rolling consists of elongation in rolling direction and thickness reduction parallel to the sheet plane normal, but no shears are involved. This strain tensor is referred to as an ideal plane strain tensor and will be used throughout the study. In the so-called full constraints (FC) Taylor-type approach [35] the imposed strain tensor is entirely transferred into each grain where it is fulfilled by crystallographic slip or twinning, respectively. Consequently, incompatibilities between

Table 1. Relaxation schemes showing the gradual degradation of the strain constraints and the ratio of the CRSS, $\lambda = \tau_{\{110\}\langle 111 \rangle} / \tau_{\{112\}\langle 111 \rangle}$

	Scheme 1 Reduction ϵ_{11} (%)		Scheme 2 Reduction ϵ_{11} (%)		Scheme 3 Reduction ϵ_{11} (%)	
	(1a) $\lambda = 1$	(1b) $\lambda = 10$	(2a) $\lambda = 1$	(2b) $\lambda = 10$	(3a) $\lambda = 1$	(3b) $\lambda = 10$
FC-model (no strain relaxation)	> 0–10	> 0–10	> 0–30	> 0–30	> 0–30	> 0–30
RC-model (lath, ϵ_{13} relaxed)	> 10–30	> 10–30	> 30–70	> 30–70	—	—
RC-model (pancake, ϵ_{13} and ϵ_{23} relaxed)	> 30–90	> 30–90	> 70–90	> 70–90	> 30–90	> 30–90

neighbouring grains are avoided. In the various variants of the so-called relaxed constraints (RC) Taylor-type approach [43, 46–48], however, some of the external shear components are not transferred into the grain, i.e. the relaxed constraints Taylor theory assumes that shear strains also occur microscopically. A relaxation of the strain component ϵ_{13} corresponds to a shear in a longitudinal direction (so-called lath model), while ϵ_{23} denotes transverse shear. The relaxation of both ϵ_{13} and ϵ_{23} is referred to as the pancake model. The axis convention is: 1 = rolling direction, 2 = transverse direction and 3 = normal direction. Allowing for these shears locally leads to distinct changes in the lattice rotation and thus in the texture development when compared to the predictions by FC theory.

The evolution of the aspect ratio of the grains during rolling is taken into account by gradually relaxing the externally imposed strain constraints with increasing deformation. For simulating low reductions, FC Taylor-type conditions are stipulated. For describing intermediate reductions, the lath model, and for large reductions, the pancake model are employed (Table 1). As was pointed out by Raphanel and van Houtte [48] this successive relaxation scheme is to a certain extent arbitrary. In the current study, hence, the influence of the relaxation

scheme on the simulation results was examined. For this purpose three modes of subsequent relaxation of ϵ_{13} and $\epsilon_{13} + \epsilon_{23}$ were used. According to scheme 1, FC conditions were employed up to a total reduction of $\epsilon = 10\%$, lath conditions between $\epsilon = 10$ and 30% and the pancake model within the range $\epsilon = 30$ –90%. In scheme 2, the FC model was applied up to $\epsilon = 30\%$, the lath model between 30 and 70% and the pancake model within the range $\epsilon = 70$ –90%. According to scheme 3, the FC model was used up to a reduction of $\epsilon = 30\%$ and the pancake model within the range $\epsilon = 30$ –90% (Table 1). In this context ϵ denotes the reduction ϵ_{11} .

For the fulfilment of the imposed strain tensor $\{110\}\langle 111 \rangle$ and $\{112\}\langle 111 \rangle$ slip systems were considered in accordance with results stemming from single crystal experiments, e.g. Refs [11, 15–17]. As was shown previously for non-ordered body centred cubic (b.c.c.) alloys [48], the asymmetry of $\{112\}\langle 111 \rangle$ slip is of minor importance and was hence neglected. For the selection of the active slip systems in the case of non-unique solutions, the second-order plastic criterion suggested by Renouard and Wintemberger [49] was applied. In contrast to former studies [40–42] the ratio of the critical resolved shear stress (CRSS) on both systems $\lambda = \tau_{\{110\}\langle 111 \rangle} / \tau_{\{112\}\langle 111 \rangle}$ was varied within the range 10–1. In the present study, the

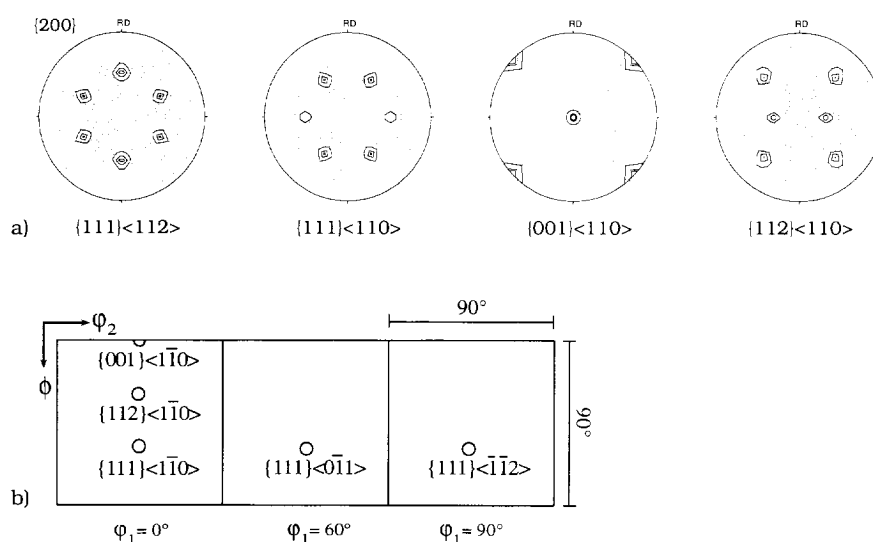


Fig. 1. Schematic presentation of some relevant texture components observed in rolled B2- and DO₃-ordered iron aluminides [38–42] and non-ordered b.c.c. metals and alloys [35, 50–52]. The textures are presented by using $\{200\}$ pole figures [Fig. 1(a)] and three ODF sections, $\phi_1 = 0^\circ$, $\phi_1 = 60^\circ$ and $\phi_1 = 90^\circ$ [Fig. 1(b)].

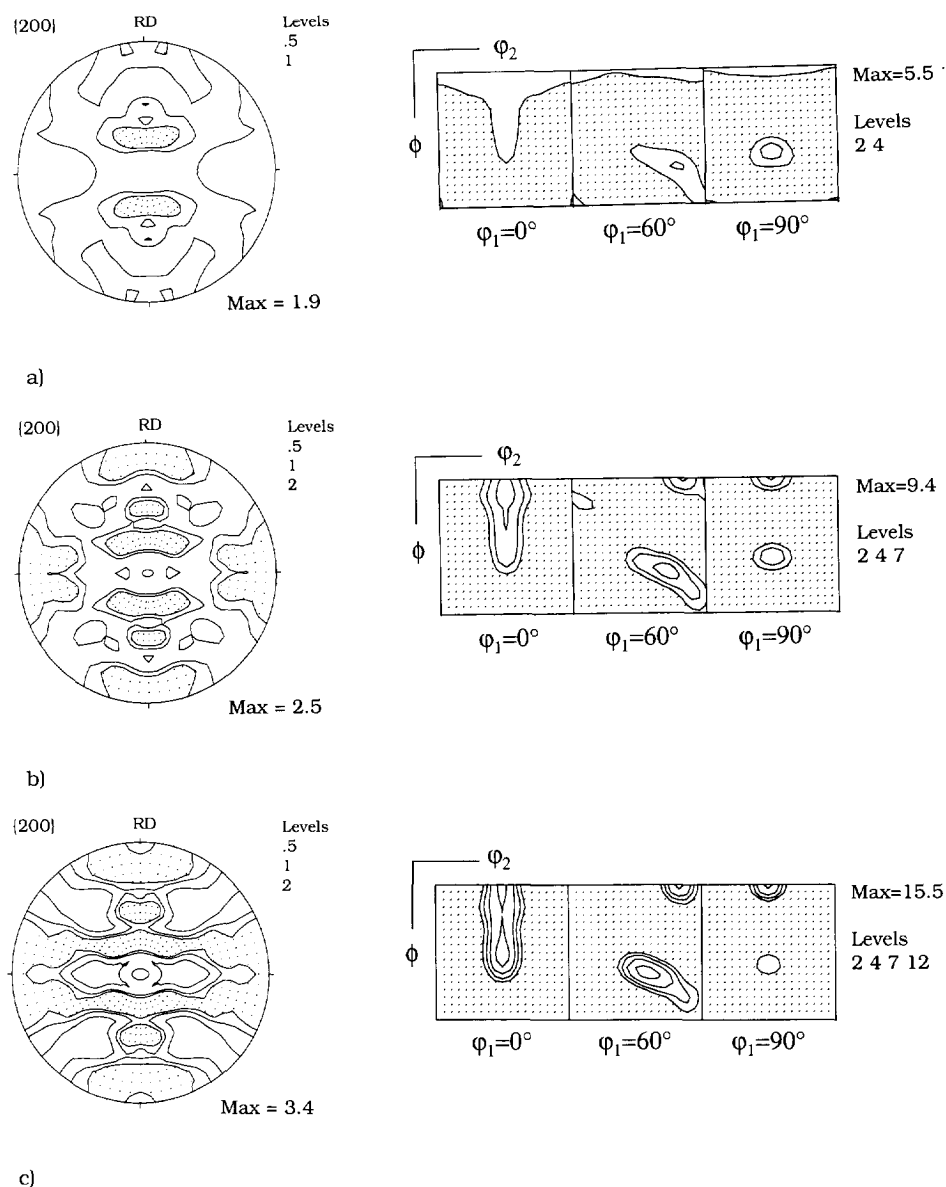


Fig. 2. Simulated development of rolled B2- and DO₃-ordered iron aluminides according to scheme 1a (Table 1): {110}<111> and {112}<111> slip, $\tau_{\{110\}\langle 111 \rangle} = \tau_{\{112\}\langle 111 \rangle}$, gradual strain relaxation: $\epsilon = 0$ –10% (FC), $\epsilon \geq 10$ –30% (RC, lath), $\epsilon \geq 30$ –90% (RC, pancake). Presentation as {200} pole figure and ODF using relevant ϕ_1 -sections: (a) $\epsilon = 30\%$; (b) $\epsilon = 60\%$; and (c) $\epsilon = 80\%$ ($\epsilon = \epsilon_{11}$).

CRSS represents a somewhat artificial value. However, comprising various influences like the nucleation of superlattice dislocations, core effects and the Peierls stress [15–17], it represents a rough measure of whether dislocations on a certain glide system contribute to slip or not. In the Taylor model employed it is not practicable to explicitly differentiate between deformation via ordinary or superlattice dislocations. This is due to the fact that in the Taylor theory, the slip systems are reduced purely to their geometrical function, i.e. the entire framework of dislocation dynamics is completely neglected. Whereas the influence of the changing aspect ratio of the grains is

artificially treated by the RC-type models, the absence of dislocation dynamics implies that effects like strain hardening, the influence of the cell sizes and the occurrence of mesoscopic inhomogeneities like micro- and shear-bands which all affect the texture development in terms of quantitative (rotation velocity, texture maximum) and qualitative deviations (stable orientations) are not taken into consideration. Consequently, the present study does not tackle the question of whether the activation of ordinary or superlattice dislocations prevails during deformation. However, it investigates whether the carriers of plastic deformation move primarily on {110} or {112} slip

planes. The simulation was carried out by the use of 936 initial randomly-distributed single orientations. For computing the resulting 3-D orientation distribution function (ODF) each orientation was superimposed by a Gauss function with a scatter width of 7° [34]. From the ODFs the centrosymmetric 2-D $\{200\}$ pole figures were additionally projected. Pole figures do not allow presentation of all relevant details of the 3-D textures because of the superposition of the types of poles considered. However, they adequately represent the main features of the texture and are thus helpful in qualitative terms.

Rolled b.c.c., e.g. Refs [50–52] and most related B2- and DO₃-ordered alloys [38–42] typically develop

strong fibre textures. Their main features can conveniently be presented using pole figures [Fig. 1(a)] or some important isointensity diagrams (φ_1 -sections) of the ODF [Fig. 1(b)]. In this study the textures are presented by using both $\{200\}$ pole figures [Fig. 1(a)] and three main ODF sections, $\varphi_1 = 0^\circ$, $\varphi_1 = 60^\circ$ and $\varphi_1 = 90^\circ$ [Fig. 1(b)].

Relevant texture components which are typically generated during rolling are positioned on the so called α -fibre which comprises all orientations with a common crystallographic $\langle 110 \rangle$ direction parallel to the rolling direction (e.g. $\{001\}\langle 110 \rangle$ at $\phi = 0^\circ$, $\{112\}\langle 110 \rangle$ at $\phi \approx 35^\circ$, $\varphi_1 = 0^\circ$ and $\{111\}\langle 110 \rangle$ at $\phi \approx 55^\circ$, $\varphi_1 = 0^\circ$) and on the so-called

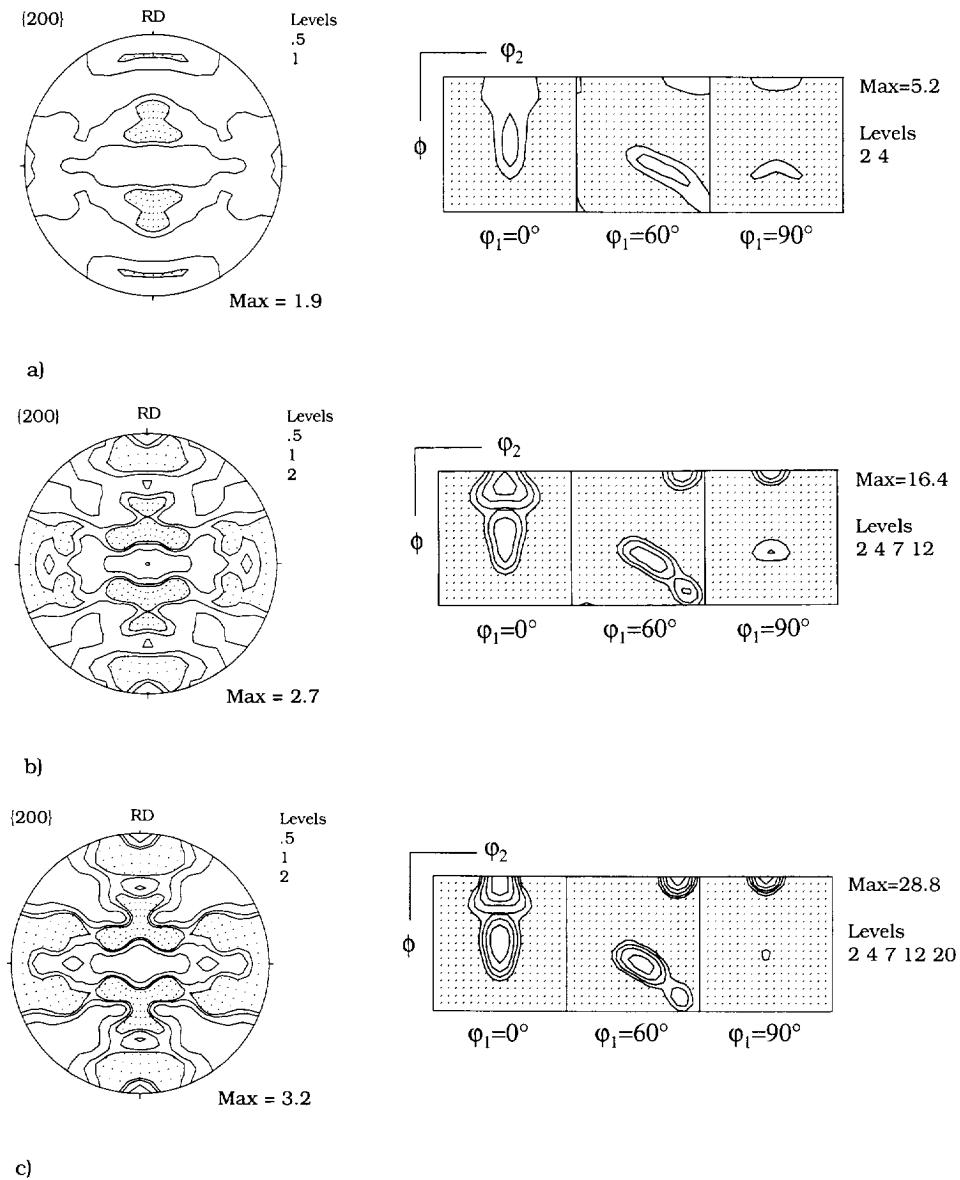


Fig. 3. Simulated development of rolled B2- and DO₃-ordered iron aluminides according to scheme 1b (Table 1): $\{110\}\langle 111 \rangle$ and $\{112\}\langle 111 \rangle$ slip, $\tau_{\{110\}\langle 111 \rangle} = 10 \times \tau_{\{112\}\langle 111 \rangle}$, gradual strain relaxation: $\epsilon = 0$ –10% (FC), $\epsilon \geq 10$ –30% (RC, lath), $\epsilon \geq 30$ –90% (RC, pancake). Presentation as $\{200\}$ pole figure and ODF using relevant φ_1 -sections: (a) $\epsilon = 30\%$; (b) $\epsilon = 60\%$; and (c) $\epsilon = 80\%$ ($\epsilon = \epsilon_{11}$).

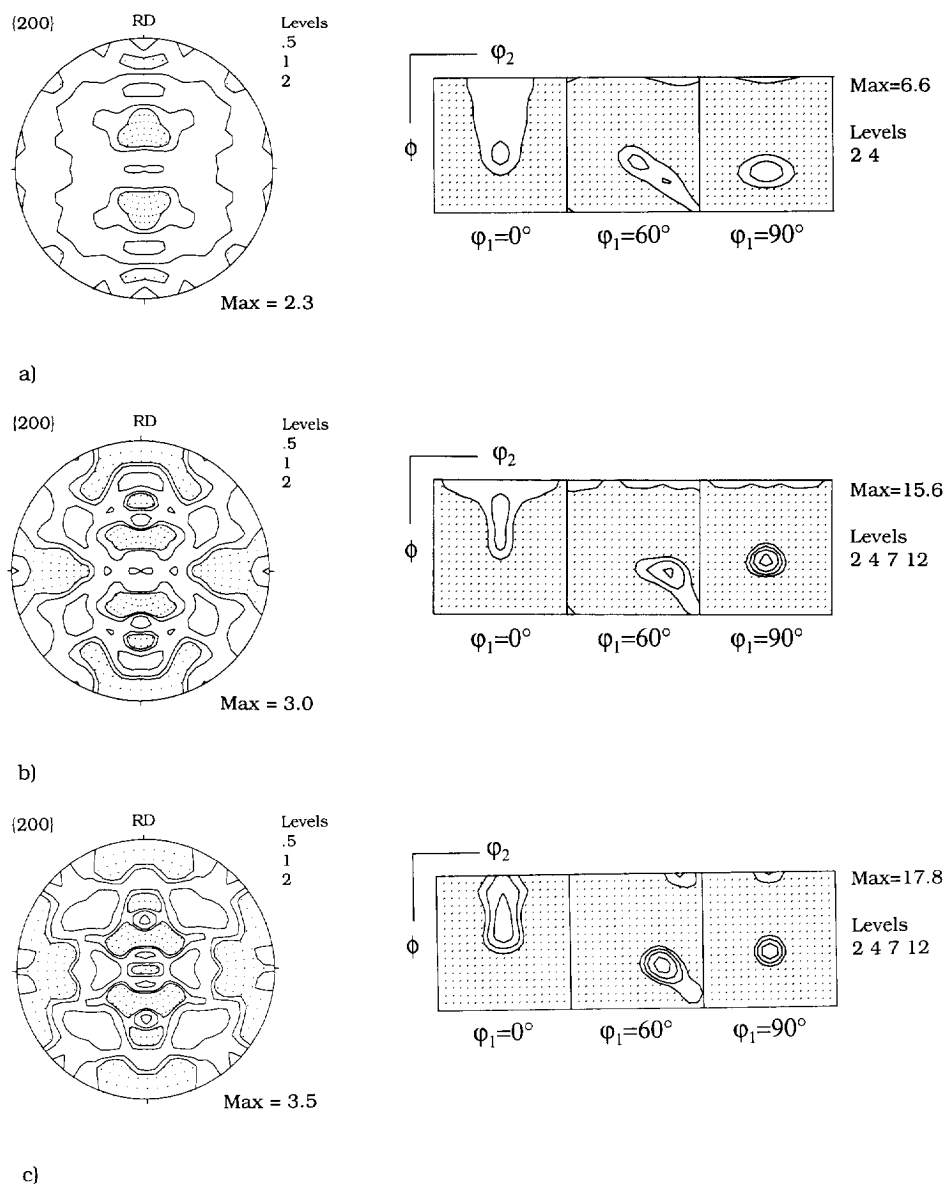


Fig. 4. Simulated development of rolled B2- and DO₃-ordered iron aluminides according to scheme 2a (Table 1): $\{110\}\langle 111 \rangle$ and $\{112\}\langle 111 \rangle$ slip, $\tau_{\{110\}\langle 111 \rangle} = \tau_{\{112\}\langle 111 \rangle}$, gradual strain relaxation: $\epsilon = 0\text{--}30\%$ (FC), $\epsilon \geq 30\text{--}70\%$ (RC, lath), $\epsilon \geq 70\text{--}90\%$ (RC, pancake). Presentation as $\{200\}$ pole figure and ODF using relevant ϕ_1 -sections: (a) $\epsilon = 30\%$; (b) $\epsilon = 60\%$; and (c) $\epsilon = 80\%$ ($\epsilon = \epsilon_{11}$).

γ -fibre containing orientations with a common $\{111\}$ plane parallel to the surface of the sheet, i.e. $\{111\}\langle 110 \rangle$ at $\phi_1 = 0^\circ$, 60° and $\{111\}\langle 112 \rangle$ at $\phi_1 = 30^\circ$, 90° [Fig. 1(b)] [38–42, 50–52].

3. SIMULATION RESULTS

Two simulations were conducted according to scheme 1 (Table 1). The first one with $\lambda = 1$, hereafter referred to as scheme 1a simulation, is depicted in Fig. 2. The second one with $\lambda = 10$, hereafter referred to as scheme 1b simulation, is shown in Fig. 3. According to scheme 1a the formation of a uniform

α -fibre ranging from a slightly pronounced $\{001\}\langle 110 \rangle$ ($\phi_1 = 0^\circ$, $\phi = 0^\circ$, $\phi_2 = 45^\circ$) to nearly $\{111\}\langle 110 \rangle$ ($\phi_1 = 0^\circ$, $\phi \approx 55^\circ$, $\phi_2 = 45^\circ$ and $\phi_1 = 60^\circ$, $\phi \approx 55^\circ$, $\phi_2 = 45^\circ$) accompanied by a $\{111\}\langle 112 \rangle$ ($\phi_1 = 90^\circ$, $\phi \approx 55^\circ$, $\phi_2 = 45^\circ$) on the γ -fibre is revealed for $\epsilon \leq 60\%$ [Figs 2(a, b)]. For $\epsilon = 80\%$ on the equally shaped α -fibre, two maximum components, one at $\{001\}\langle 110 \rangle$ and one close to $\{111\}\langle 110 \rangle$ at $\phi \approx 48^\circ$ are generated. On the γ -fibre the maximum is stabilised at $\{111\}\langle 110 \rangle$, whereas $\{111\}\langle 112 \rangle$ is degraded [Fig. 2(c)].

Scheme 1b simulation leads to a different prediction (Fig. 3). At low reductions [Fig. 3(a)] a uniform

α -fibre and a very weak γ -fibre are formed. At elevated reductions [Figs 3(b, c)], two isolated components are formed on the α -fibre, whilst the γ -fibre, especially the $\{111\}\langle 112\rangle$, is completely degraded. At reductions within the range $\epsilon = 60\text{--}80\%$ the first strong maximum is located close to $\{001\}\langle 110\rangle$ and the second one close to $\{223\}\langle 110\rangle$ [Fig. 3(c)].

The two simulations which were conducted in accord with scheme 2 are named scheme 2a ($\lambda = 1$) and scheme 2b ($\lambda = 10$) simulation (Figs 4, 5). At low reductions, $\epsilon = 30\%$ [Figs 4(a), 5(a)], both simulations predict a uniform α -fibre ranging from $\{001\}\langle 110\rangle$ to a slightly pronounced $\{111\}\langle 110\rangle$ and

a γ -fibre. At larger reductions, scheme 2a simulation leads to a non-uniformly shaped α -fibre with a maximum at $\{112\}\langle 110\rangle$ which is accompanied by a $\{111\}\langle 112\rangle$ component on the γ -fibre [Figs 4(b, c)]. In the same regime ($\epsilon = 60$ and 80%) the scheme 2b model predicts a strong maximum close to $\{112\}\langle 110\rangle$ and the total decrease of the γ -fibre, especially of the $\{111\}\langle 112\rangle$ orientation [Figs 5(b, c)].

The two simulations which were executed following scheme 3 are hereafter referred to as scheme 3a ($\lambda = 1$) and scheme 3b ($\lambda = 10$) models, respectively (Figs 6, 7). Employing, scheme 3a's approach, a uniformly shaped α -fibre with a maximum at

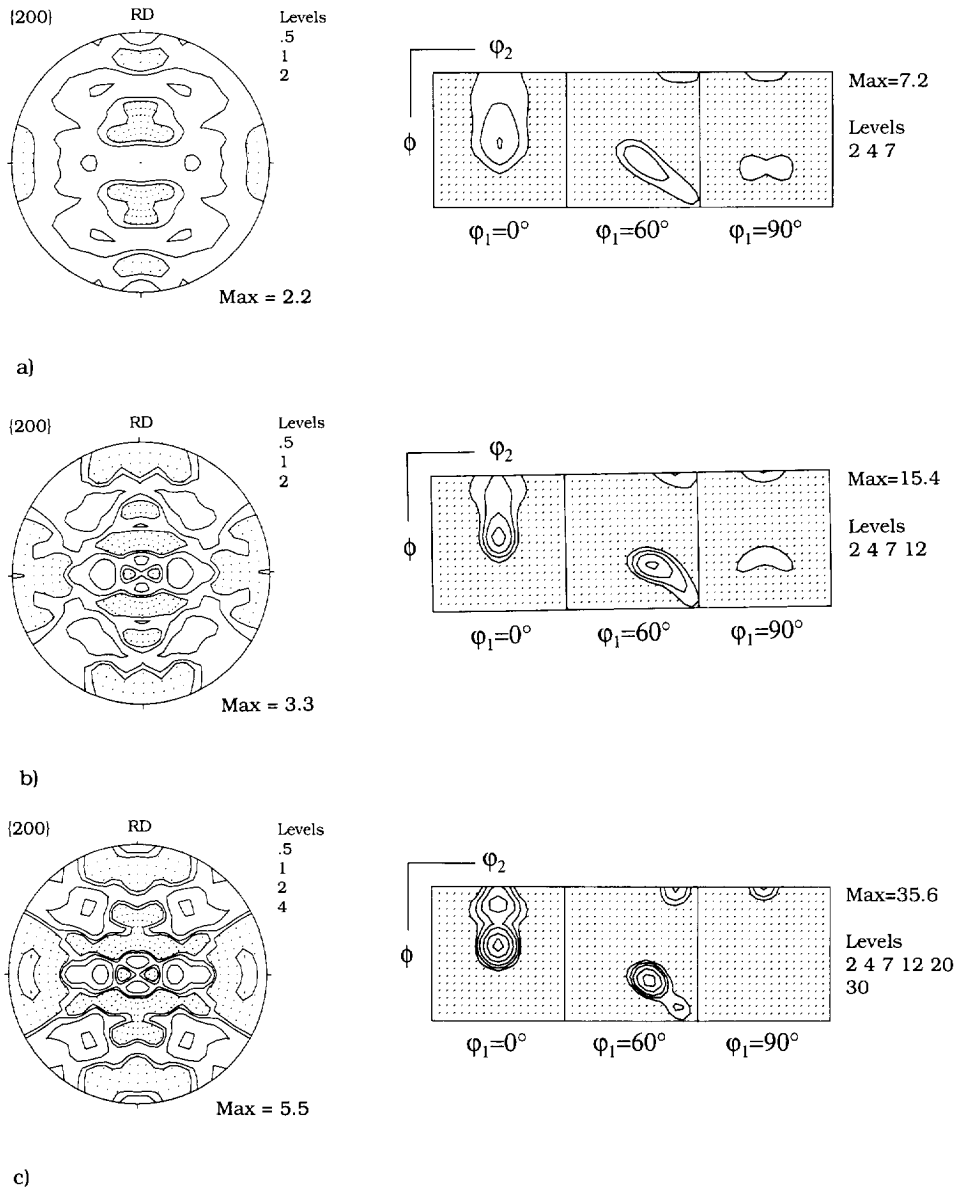


Fig. 5. Simulated development of rolled B2- and DO₃-ordered iron aluminides according to scheme 2b (Table 1): $\{110\}\langle 111\rangle$ and $\{112\}\langle 111\rangle$ slip, $\tau_{\{110\}\langle 111\rangle} = 10 \times \tau_{\{112\}\langle 111\rangle}$, gradual strain relaxation: $\epsilon = 0\text{--}30\%$ (FC), $\epsilon \geq 30\text{--}70\%$ (RC, lath), $\epsilon \geq 70\text{--}90\%$ (RC, pancake). Presentation as $\{200\}$ pole figure and ODF using relevant ϕ_1 -sections: (a) $\epsilon = 30\%$; (b) $\epsilon = 60\%$; and (c) $\epsilon = 80\%$ ($\epsilon = \epsilon_{11}$).

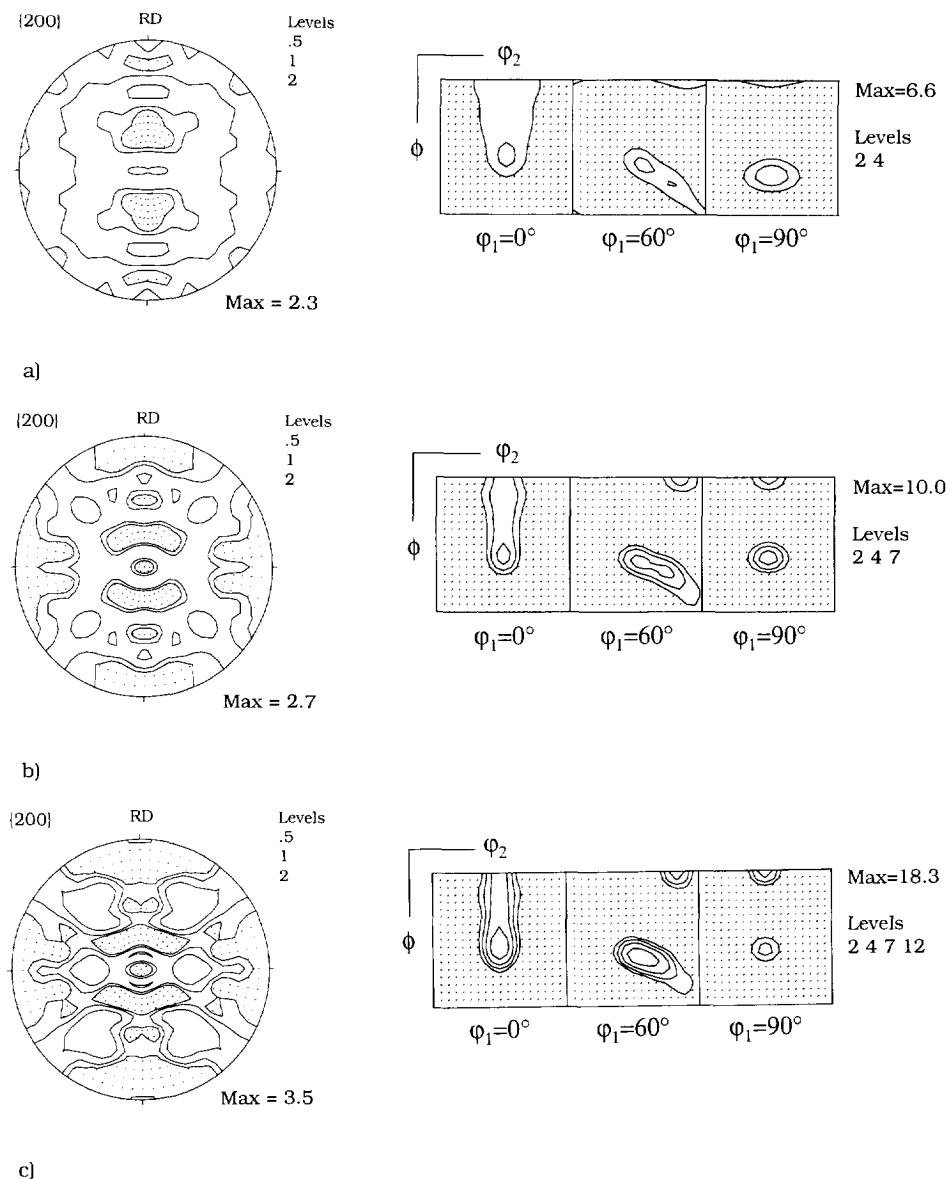


Fig. 6. Simulated development of rolled B2- and DO₃-ordered iron aluminides according to scheme 3a (Table 1): {110}<111> and {112}<111> slip, $\tau_{\{110\}\langle 111 \rangle} = \tau_{\{112\}\langle 111 \rangle}$, gradual strain relaxation: $\epsilon = 0$ –30% (FC), $\epsilon \geq 30$ –90% (RC, pancake). Presentation as {200} pole figure and ODF using relevant ϕ_1 -sections: (a) $\epsilon = 30\%$; (b) $\epsilon = 60\%$; and (c) $\epsilon = 80\%$ ($\epsilon = \epsilon_{11}$).

{111}<110> is predicted (Fig. 6). On the regularly formed γ -fibre an orientation tube ranging from the pronounced {111}<110> orientation to a weaker component close to {111}<112> is revealed (Fig. 6). The scheme 3b simulation (Fig. 7) bears a certain resemblance to the scheme 1b prediction (Fig. 3). At low reductions [Fig. 7(a)], a uniform α -fibre and a weak γ -fibre are generated. At larger reductions [Figs 7(b,c)] two single components are formed on the α -fibre whilst the γ -fibre, especially the {111}<112>, is weakened. At $\epsilon = 80\%$ one strong maximum is located close to {001}<110> and a second one between {223}<110> and {111}<110> [Fig. 7(c)].

4. EXPERIMENTAL PROCEDURE AND RESULTS

A cast intermetallic Fe₃Al alloy with 15.7% Al, 0.088% Cr, <0.05% Zr, 0.02% Mo and 0.06% C (% = mass%) was thermomechanically hot rolled to a final thickness of 4.86 mm and finally annealed at 870 K. The latter two manufacturing steps are referred to as B2 treatment [13, 14]. Subsequently, the sheet was rolled at 800–830 K to $\epsilon = 80\%$. The final sheet had an imperfectly-oriented B2 structure [13, 14]. Recrystallisation was not observed. The microstructure of the rolled samples was studied by means of optical and electron microscopy. For this

purpose the specimens were etched in pure HCl (1–3 min) in the case of low deformation and in a solution of 10 ml H_2O_2 and 1 ml HF (30 s) in the case of large reductions ($\epsilon \geq 70\%$).

The textures were measured in the centre layer of the specimens. For this purpose the samples were ground and finally etched by use of pure HCl. The experiments were carried out on an X-ray texture goniometer using $\text{Mo}_{K\alpha}$ radiation. The four incomplete pole figures: $\{220\}$, $\{400\}$, $\{422\}$ and $\{620\}$ were measured within the range of the pole distance angle $\alpha = 5^\circ\text{--}85^\circ$ in the back reflection mode [53]. From the 2-D, centrosymmetric pole figures the quantitative 3-D ODF was computed using the iterative series expansion procedure ($I_{\text{max}} = 22$) [54–56].

Figure 8 shows the starting texture, i.e. the orientation distribution after casting, thermomechanical hot rolling and final heat treatment. The maximum occurring orientation density is quite small, $f(g)_{\text{max}} = 6.8$. The ODF reveals two main initial texture components, viz. an orientation located between the $\{112\}\langle 110\rangle$ and the $\{111\}\langle 110\rangle$ component, and a $\{001\}\langle 110\rangle$ orientation. Additionally, a weak γ -fibre appears. In the corresponding microstructure essentially equiaxed or slightly elongated grains were found which suggests that recrystallisation has taken place during or subsequent to the thermomechanical treatment (Fig. 9).

After 30% reduction the texture reveals a dominant component close to $\{111\}\langle 110\rangle$, a weak

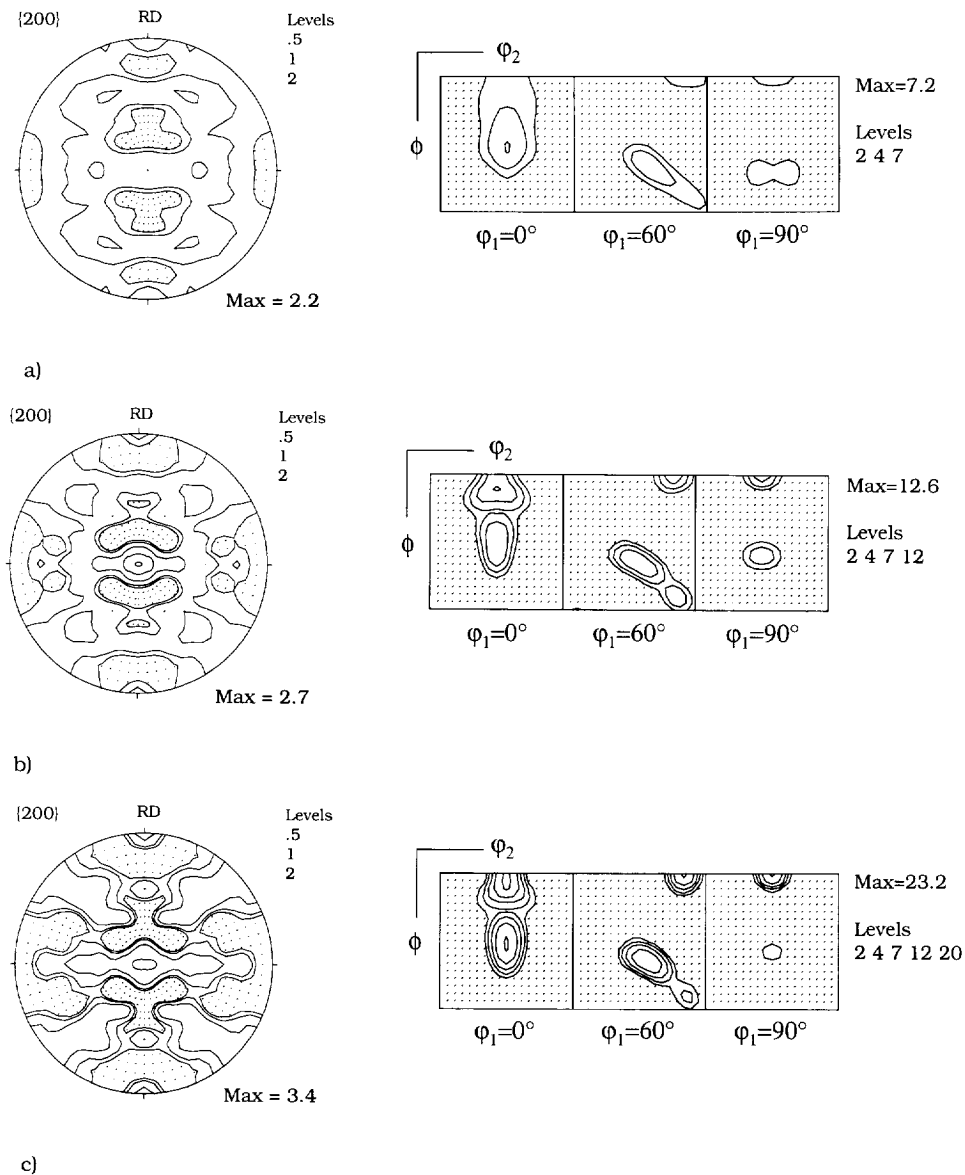


Fig. 7. Simulated development of rolled B2- and DO_3 -ordered iron aluminides according to scheme 3b (Table 1): $\{110\}\langle 111\rangle$ and $\{112\}\langle 111\rangle$ slip, $\tau_{\{110\}\langle 111\rangle} = 10 \times \tau_{\{112\}\langle 111\rangle}$, gradual strain relaxation: $\epsilon = 0\text{--}30\%$ (FC), $\epsilon \geq 30\text{--}90\%$ (RC, pancake). Presentation as $\{200\}$ pole figure and ODF using relevant ϕ_1 -sections: (a) $\epsilon = 30\%$; (b) $\epsilon = 60\%$; and (c) $\epsilon = 80\%$ ($\epsilon = \epsilon_{11}$).

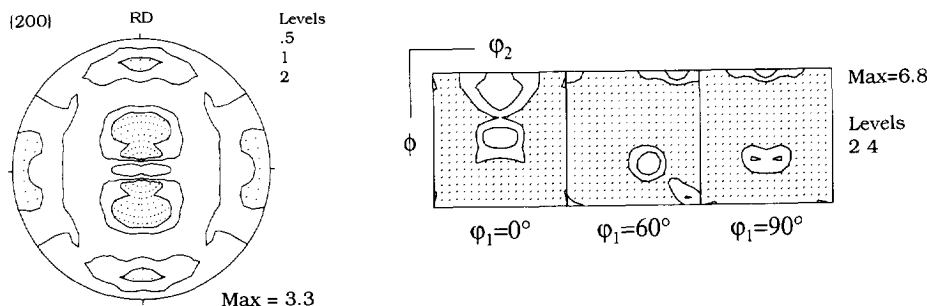


Fig. 8. Experimental starting texture (cast, thermomechanical hot rolled and finally annealed at 870 K) in the centre layer, orientation distribution function (ODF) calculated by use of the iterative series expansion method ($I_{\max} = 22$) [54–56]. Presentation as $\{200\}$ pole figure and ODF using relevant ϕ_1 -sections.

$\{001\}\langle 110 \rangle$ orientation and an equally shaped γ -fibre consisting of $\{111\}\langle 110 \rangle$ and $\{111\}\langle 112 \rangle$ [Fig. 10(a)]. The $\{112\}\langle 110 \rangle$ orientation which was inherited from the starting texture rotated towards the $\{111\}\langle 110 \rangle$ component. This type of texture, especially the minimum at $\{112\}\langle 110 \rangle$ is typical of rolling textures of B2-ordered alloys [38–42]. However, it is not typical of rolled non-ordered b.c.c. compounds which reveal a texture maximum at $\{112\}\langle 110 \rangle$ rather than a minimum [50–52].

With increasing rolling deformation, $\epsilon = 60\%$ [Fig. 10(b)] and $\epsilon = 80\%$ [Fig. 10(c)], the γ -fibre gradually increases. The orientation density of the $\{001\}\langle uvw \rangle$ texture fibre, especially of the $\{001\}\langle 110 \rangle$ component remains very weak. The formation of a $\{111\}\langle uvw \rangle$ texture fibre is well known from cold-rolled non-ordered b.c.c. alloys [50–52]. However, at large strains in these materials the γ -fibre is accompanied by an equally shaped α -fibre, especially by a $\{001\}\langle 110 \rangle$ and a dominant $\{112\}\langle 110 \rangle$ component. The rolled Fe_3Al specimen reveals a weak $\{001\}\langle 110 \rangle$ orien-

tation, but the $\{112\}\langle 110 \rangle$ component does not appear at all. Although an orientation close to $\{112\}\langle 110 \rangle$ was present in the initial texture (Fig. 8) it decreases during subsequent cold rolling rather than stabilises (Fig. 10).

5. DISCUSSION

The Taylor simulations (Figs 2–7) can either be discussed in terms of the type of gradual strain relaxation (Table 1) or in terms of the ratio of the critical resolved shear stress (CRSS) on both systems $\lambda = \tau_{\{110\}\langle 111 \rangle} / \tau_{\{112\}\langle 111 \rangle}$ which was either 1 or 10. From the simulation results, the latter approach is suggested. Both the simulations which were carried out with $\lambda = 1$ (Figs 2, 4, 6) and with $\lambda = 10$ (Figs 3, 5, 7) bear a strong resemblance among each other. The first group containing scheme 1a (Fig. 2), scheme 2a (Fig. 4) and scheme 3a (Fig. 6) approaches is hereafter named type A simulation ($\lambda = 1$). The second group containing scheme 1b (Fig. 3), scheme 2b (Fig. 5) and scheme 3b (Fig. 7) approaches is



Fig. 9. Longitudinal section of the material after casting, thermomechanical hot rolling and subsequent annealing at 870 K.

hereafter named type B simulation ($\lambda = 10$). The textures predicted by the type A approach ($\tau_{\{110\}\langle 111 \rangle} = \tau_{\{112\}\langle 111 \rangle}$) reveal the following common characteristics:

Type A. The α -fibre reveals a fairly homogeneous shape between $\{001\}\langle 110 \rangle$ and $\{112\}\langle 110 \rangle$ (Fig. 4) or $\{111\}\langle 110 \rangle$, respectively (Figs 2, 6). The γ -fibre reveals a quite homogeneous shape with a maximum either at $\{111\}\langle 110 \rangle$ (Figs 2, 6) or at $\{111\}\langle 112 \rangle$ (Fig. 4). The maximum occurring orientation densities after $\epsilon = 80\%$ are within the range $f(g)_{\max} = 15.5\text{--}18.3$, i.e. they are generally lower than for the type B simulations. The textures predicted bear a considerable resemblance to the textures of

non-ordered b.c.c. alloys [50–52]. The relaxation schemes employed seem to be of secondary importance. However, the approaches which make use of the pancake model already at low strains, $\epsilon \geq 30\%$, viz. scheme 1 (Fig. 2) and scheme 3 (Fig. 6), yield a somewhat better agreement with b.c.c. rolling textures [50–52] than the scheme 2 approach (Fig. 4). From the analysis of the amount of shear contributed by the various types of slip systems it is revealed that orientations close to $\{112\}\langle 110 \rangle$ and $\{111\}\langle 112 \rangle$ are essentially stabilised by $\{110\}\langle 111 \rangle$ slip systems. Orientations close to $\{001\}\langle 110 \rangle$ and $\{111\}\langle 110 \rangle$ are stabilised by both $\{110\}\langle 111 \rangle$ and $\{112\}\langle 111 \rangle$ glide systems.

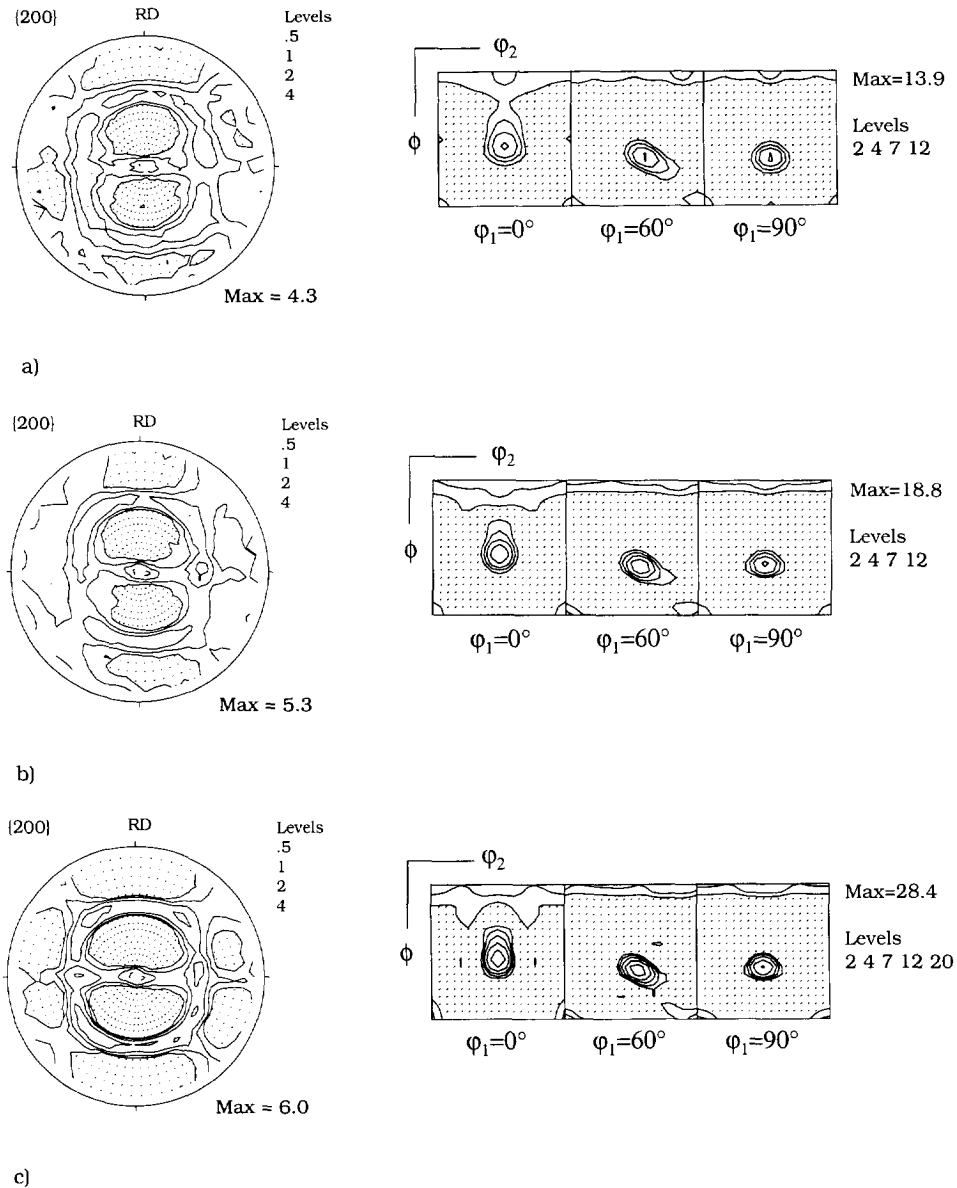


Fig. 10. Experimental rolling textures in the centre layer ($T_{\text{roll}} = 800\text{--}830\text{ K}$), orientation distribution function (ODF) calculated by use of the iterative series expansion method ($I_{\max} = 22$) [54–56]. Presentation as {200} pole figure and ODF using relevant ϕ_1 -sections: (a) $\epsilon = 30\%$; (b) $\epsilon = 60\%$; and (c) $\epsilon = 80\%$ ($\epsilon = \epsilon_1$).

In contrast, the textures predicted by the type B approach ($\tau_{\{110\}\langle 111 \rangle} = 10 \times \tau_{\{112\}\langle 111 \rangle}$) are all characterised by the following features:

Type B. The α -fibre is not uniformly shaped but reveals two distinct maximum components, one close to $\{001\}\langle 110 \rangle$ and one close to $\{112\}\langle 110 \rangle$ (Fig. 5) or $\{223\}\langle 110 \rangle$, respectively (Figs 3, 7). The γ -fibre is usually very weak (Fig. 5) or reduced to a weak component close to $\{111\}\langle 110 \rangle$ (Figs 3, 7). The maximum occurring orientation densities after $\epsilon = 80\%$ are in all cases higher than for the type A simulations. They are within the range $f(g)_{\max} = 23.2\text{--}35.6$. The textures predicted bear little resemblance to the textures of non-ordered b.c.c. alloys [50–52]. The formation of a strong $\{001\}\langle 110 \rangle$ texture component is promoted by the dominance of $\{112\}\langle 111 \rangle$ slip. The relaxation schemes employed seem to be of minor relevance. Due to the high CRSS on the $\{110\}\langle 111 \rangle$ slip systems the shear is exclusively contributed by the $\{112\}\langle 111 \rangle$ slip systems.

From the features discussed above it appears that the type B approach ($\{112\}$ slip planes), especially schemes 1b and 3b, yields a better agreement with experiment (Fig. 10) than the type A approach ($\{110\}$ and $\{112\}$ slip planes). Although the orientation density of the $\{001\}\langle 110 \rangle$ and of the $\{111\}\langle 112 \rangle$ component is not correctly predicted at large reductions (Figs 3, 7) the absence of the $\{112\}\langle 110 \rangle$ orientation which usually dominates the rolling textures of non-ordered b.c.c. alloys [50–52] seems to be an important indicator for the prevalence of the $\{112\}\langle 111 \rangle$ slip. The $\{112\}\langle 110 \rangle$ component is stabilised by pure $\{110\}\langle 111 \rangle$ slip and generally destabilised by pure $\{112\}\langle 111 \rangle$ slip. This is not only shown by the complex models employed in this study but also covered by a simple Sachs type approach [57] under double slip conditions. Applying the latter model with pure $\{112\}\langle 111 \rangle$ slip predicts a $\{332\}\langle 110 \rangle$ component. This solution approximately corresponds to the stable orientation between $\{223\}\langle 110 \rangle$ and $\{111\}\langle 110 \rangle$ which is predicted by two type B simulations (Figs 3, 7) and which is observed experimentally (Fig. 10). Whereas a typical b.c.c. rolling texture contains two fibres, viz. α - and γ -fibres, the typical B2 or, respectively, DO₃ texture only contains one fibre, namely the γ -fibre or at least a fibre close to that (so-called β -fibre). Since the crystallographic texture is directly connected to the activated slip systems it may hence be concluded that $\{110\}\langle 111 \rangle$ glide systems do not play the leading role for the plastic deformation of B2 and DO₃ ordered polycrystals.

However, this observation does not mean that plastic deformation of such compounds is exclusively attained by activation of $\{112\}\langle 111 \rangle$ glide systems. This qualification is supported by the evolution of the orientation density of both the $\{001\}\langle 110 \rangle$ and of the $\{111\}\langle 112 \rangle$ texture components. Their development during rolling (Fig. 10) is not adequately covered by

the scheme B simulations (Figs 3, 7). Whereas the orientation density of the $\{001\}\langle 110 \rangle$ component is overestimated by the type B models, that of the $\{111\}\langle 112 \rangle$ component is underestimated when compared to the experiment (Fig. 10). This observation substantiates that $\{110\}\langle 111 \rangle$ glide systems may indeed contribute at least a minor portion to the deformation of certain texture components. As will be discussed at the end of this section, such transition between both types of slip as a function of temperature, strain rate and grain orientation is also conceivable from an atomistic point of view.

The second result which requires some consideration is the influence of the various relaxation schemes on the resulting texture (Table 1). It is evident that the incorporation of the pancake model already at low reductions, $\epsilon \geq 30\%$, scheme 1 (Fig. 3) and scheme 3 (Fig. 7) leads to a better agreement with experiment than its incorporation at large reductions, $\epsilon \geq 70\%$ (Fig. 5). At first sight this indicates a strong influence of the grain shape. However, Fig. 9 shows that the aspect ratio of the initial grains ($\epsilon = 0\%$) is close to 1, i.e. the crystals are only slightly elongated at low reductions. Furthermore, the consideration of grain shape via successive relaxation of strain constraints is generally a coarse approximation and to a certain extent arbitrary. For any sound physical approach which aims to incorporate local strain relaxation, the local texture and morphology must be known [58, 59]. Consequently, in the present case an argumentation in terms of morphology is not convincing.

However, the relaxation of two strain constraints, viz. of ϵ_{13} and ϵ_{23} , leads to a decrease in the number of active slip systems from five to three. This results in the degradation of the corresponding deformation energy, which is computed by $\tau_{\{112\}\langle 111 \rangle} \cdot M$, where $\tau_{\{112\}\langle 111 \rangle}$ is the CRSS on $\{112\}\langle 111 \rangle$ slip systems and M the Taylor factor. In a rough approach, the local accomplishment of shear strains between two neighbouring grains may be regarded in terms of two conflicting energies. The first one is the gain of energy that is achieved by relaxing strains locally. The decrease of the number of active slip systems from 5 (FC) to 3 (RC) leads to a degradation of the corresponding Taylor energy. This portion is described by the difference of the deformation energy predicted by the FC and RC models, i.e. $t \cdot (M_{\text{FC}} - M_{\text{RC}})$. The gain in deformation energy is hence linearly proportional to the CRSS. However, the relaxation of strain constraints locally may lead to geometrical incompatibility between the grains. The competitive term which must hence be balanced by the gain in Taylor energy is the elastic energy which is required to compensate this incompatibility. It may be described as non-localised in terms of an elastic strain accommodation energy [60] or localised in terms of geometrically necessary dislocations [58, 61]. Due to this balance it is conceivable that if the CRSS increases, e.g. through the generation of



Fig. 11. Longitudinal section of an 80% rolled specimen ($T_{\text{roll}} = 800\text{--}830\text{ K}$). In numerous grains straight slip lines were observed.

ABP, and if the elastic accommodation energy remains unchanged, it is energetically more favourable to decrease the number of active slip systems, i.e. to relax strain constraints locally, than to avoid incompatibilities by activating five slip systems. Such argument seems physically reasonable since in ordered alloys a large glide resistance, i.e. a large Taylor energy must be considered due to the energy of the APB, core effects and the Peierls stress [8, 15–17]. The presence of superlattice dislocations in the deformed samples is indeed suggested by the slip traces which were observed in the longitudinal sections of many grains (Fig. 11). These traces were usually straight rather than wavy [8, 11, 17, 31, 32].

Finally, a third argument, namely the starting texture must be taken into account when discussing the success of the pancake-type models. From Fig. 8 it is evident that some important features of the final texture (Fig. 10) are already present prior to the final rolling procedure. The initial texture maximum close to $\{112\}\langle 110 \rangle$ which is not stable under $\{112\}\langle 111 \rangle$ slip conditions has a disorientation of about 15° with respect to the $\{111\}\langle 110 \rangle$ orientation and about 30° with respect to the $\{111\}\langle 112 \rangle$ orientation. It is likely that the initial $\{112\}\langle 110 \rangle$ texture component rotates towards the $\{111\}\langle 110 \rangle$ orientation and hence additionally promotes the increase of the γ -fibre during rolling.

Concluding prevalence of $\{112\}\langle 111 \rangle$ rather than of $\{110\}\langle 111 \rangle$ slip from the comparison of predicted and experimentally observed textures represents a phenomenological approach. A supplementary direct result was achieved by the employment of single orientation determination in the SEM [62, 63]. By determination of the vectors of the slip markings together with the grain orientation the traces of the slip planes were computed in lattice coordinates. In

these experiments a large portion of $\{112\}$ slip planes and a minor contribution of $\{110\}$ slip planes were identified. A thorough analysis of the data will be given in a subsequent paper.

Finally, it remains an open question why $\{112\}\langle 111 \rangle$ slip prevails whilst $\{110\}\langle 111 \rangle$ slip is impeded. The generation and the movement of superlattice dislocations in B2- and DO_3 -ordered alloys with a constant order parameter is essentially governed by two lattice properties. First, by the energy of the APB, which affects the nucleation and interaction [8–10, 21] and second, by the dislocation core structure [15–17, 29] which affects the mobility of superlattice dislocations. Following Umakoshi *et al.* [15–17] and Takeuchi [29] the dislocation core of superpartials in the B2 lattice has a similar structure as in ordinary screw dislocations in the b.c.c. lattice. That means in the case of $\{110\}\langle 111 \rangle$ superlattice dislocations the cores of the corresponding superpartials are extended on three intersecting $\{110\}$ planes where they create faults. The cores are oriented in such a way that they do not overlap the APB. As in non-planar b.c.c. dislocations the three intersecting $\{110\}$ layer faults extend on the $\{112\}$ planes at their tips. As reported by Umakoshi *et al.* [15–17], the energy of the APB of $a/2\{110\}\langle 111 \rangle$ dislocations is lower compared to $a/2\{112\}\langle 111 \rangle$ superpartials. However, their core is most likely more extended than that of $a/2\{112\}\langle 111 \rangle$ dislocations. For the movement, the dislocation core must therefore first be converted into a planar configuration which increases the glide resistance. In contrast, $a/2\{112\}\langle 111 \rangle$ superpartials create intricate multi-layer faults which advocate the assumption that their dislocation cores are smaller. Although they have a higher APB energy than $\{110\}\langle 111 \rangle$ dislocations their cores can easily transform into a glissile configuration prior to the net

movement. This causes an altogether lower glide resistance compared to the $a/2\{110\}\langle 111\rangle$ dislocations. It is thus assumed that the strong tendency for $\{112\}$ slip cannot be interpreted in terms of the APB energy but in terms of dislocation core effects [15–17].

6. CONCLUDING REMARKS

The texture evolution during rolling of B2- or DO₃-ordered polycrystalline iron aluminides was described by Taylor-type simulations and compared with experimental results. In the simulations, $\{110\}\langle 111\rangle$ and $\{112\}\langle 111\rangle$ slip systems were considered. The ratio of the CRSS on both systems $\lambda = \tau_{\{110\}\langle 111\rangle} / \tau_{\{112\}\langle 111\rangle}$ was assumed to be 1 or 10, respectively. The evolution of the grain shape during rolling was considered by gradually relaxing the external strain constraints with increasing deformation. The simulations with $\lambda = 10$ (activation of $\{112\}$ slip planes) yielded a better agreement with experiment than the simulations with $\lambda = 1$ (activation of $\{110\}$ and $\{112\}$ slip planes). The predominance of $\{112\}\langle 111\rangle$ slip was discussed in terms of the energy of the APB and of dislocation core effects. The incorporation of the pancake model already at low reductions, $\epsilon \geq 30\%$ showed a better correspondence to experiment than its incorporation at large reductions, $\epsilon \geq 70\%$. The accomplishment of strain by only three slip systems was attributed to the large glide resistance in ordered alloys. It was assumed that it is energetically more favourable to decrease the number of active slip systems than to avoid strain incompatibilities.

Acknowledgements—The author gratefully acknowledges the kind support by the University of Science and Technology, Beijing, China, especially by Professor Dr Z. Sun and Professor Dr W. Mao. The Fe₃Al alloy used in this study was cast and thermomechanically processed at the Department of Materials Science and Engineering at the University of Science and Technology, Beijing.

REFERENCES

1. N. Ziegler, *Trans. AIME* **100**, 267 (1932).
2. W. Justusson, V. F. Zackay and E. R. Morgan, *Trans. Amer. Soc. Metals* **49**, 905 (1957).
3. F. Lihl and R. Stickler, *Archiv Eisenhüttenwesen* **31**, 47 (1960).
4. A. Lawley, E. A. Vidoz and R. W. Cahn, *Acta metall.* **9**, 287 (1961).
5. N. S. Stoloff and R. G. Davies, *Acta metall.* **12**, 473 (1964).
6. N. S. Stoloff and R. G. Davies, *Prog. Mater. Sci.* **13**, 1 (1966).
7. H. J. Leamy, E. D. Gibson and F. X. Kayser, *Acta metall.* **15**, 1827 (1967).
8. H. J. Leamy and F. X. Kayser, *Phys. stat. solidi* **34**, 765 (1969).
9. H. J. Leamy, F. X. Kayser and M. J. Marcinkowski, *Phil. Mag.* **20**, 763 and 779 (1969).
10. H. J. Leamy, *Acta metall.* **15**, 1839 (1967).
11. C. G. McKamey, J. H. De Van, P. F. Tortorelli and V. K. Sikka, *J. Mater. Res.* **6**, 1779 (1991).
12. C. G. McKamey and J. A. Horton, *Metall. Trans. A* **20**, 751 (1989).
13. Z. Sun, Y. Huang, R. Yang and G. Chen, in *High Temperature Ordered Intermetallic Alloys V* (edited by I. Baker, R. Darloia, J. D. Whittenberger and M. Yoo). *Mater. Res. Symp. Proc.*, Pittsburgh, p.885 (1994).
14. Z. Sun, Y. Huang, W. Yang and G. Chen, *Proc. Confer. of High Temp. Properties of Iron Based Aluminides*. TMS, San Francisco (1994).
15. Y. Umakoshi and M. Yamaguchi, *Phil. Mag.* **A41**, 573 (1980).
16. Y. Umakoshi and M. Yamaguchi, *Phil. Mag.* **A44**, 711 (1981).
17. Y. Umakoshi, in *Material Science and Technology* (edited by R. W. Cahn, P. Haasen and E. J. Kramer) Vol. 6, p. 251 VCH (1993).
18. L. Guttman, H. C. Schnyders and G. J. Arai, *Phys. Rev. Lett.* **22**, 520 (1969).
19. G. Lütjering and H. Warlimont, *Acta metall.* **12**, 1460 (1964).
20. G. Lütjering and H. Warlimont, *Z. Metallkunde* **56**, 1 (1965).
21. M. J. Marcinkowski and H. J. Leamy, *Phys. stat. solidi* **24**, 149 (1967).
22. M. J. Marcinkowski and N. Brown, *Acta metall.* **9**, 764 (1961).
23. M. J. Marcinkowski and N. Brown, *J. appl. Phys.* **33**, 537 (1962).
24. M. J. Marcinkowski and N. Chessin, *Phil. Mag.* **10**, 837 (1964).
25. M. J. Marcinkowski, in *Electron Microscopy and Strength of Crystals*, p. 333. Interscience, New York (1963).
26. W. A. Rachinger and A. H. Cottrell, *Acta metall.* **4**, 109 (1956).
27. T. Taoka and S. Sakata, *Acta metall.* **5**, 19 (1957).
28. T. Taoka and R. Honda, *J. Electronmicroscopy (Tokyo)* **5**, 19 (1957).
29. S. Takeuchi, *Proc. 5th Int. Conf. on Strength of Met. and Alloys* (edited by P. Haasen, V. Gerold and G. Kostorz) Aachen, p. 53 (1979).
30. I. Baker and D. I. Gaydos, *Mater. Sci. Engng* **96**, 147 (1987).
31. R. C. Crawford and I. L. F. Ray, *Phil. Mag.* **35**, 549 (1977).
32. S. Hanada, *Met. Technol.* **54**, 17 (1984).
33. H. J. Bunge, *Texture Analysis in Materials Science*. Butterworths, London (1982).
34. K. Lücke, J. Pospiech, K. H. Virnich and J. Jura, *Acta metall.* **29**, 167 (1981).
35. G. I. Taylor, *J. Inst. Metal.* **62**, 307 (1938).
36. D. Raabe, *Acta metall.* **43**, 1023 (1995).
37. D. Raabe, *Acta metall.* **43**, 1531 (1995).
38. W. Mao and Z. Sun, *Scripta metall.* **29**, 217 (1993).
39. W. Mao and Z. Sun, *Proc. 10th Int. Conf. on Tex. of Mat. ICOTOM 10, Materials Science Forum* **157–162**, 1009 (1994).
40. D. Raabe, *Mater. Lett.* **19**, 75 (1994).
41. D. Raabe and W. Mao, *Phil. Mag. A* **71**, 805 (1995).
42. D. Raabe, *Comp. Mater. Sci.* **3**, 231 (1994).
43. U. F. Kocks and H. Chandra, *Acta metall.* **30**, 695 (1982).
44. E. Aernoudt, *Proc. 5th Int. Conf. on Tex. of Mat. ICOTOM 5* (edited by G. Gottstein and K. Lücke), p. 45. Springer Verlag, New York (1978).
45. R. J. Asaro, *Acta metall.* **27**, 445 (1979).
46. H. Honneff and H. Mecking, *Proc. 5th Int. Conf. on Tex. of Mat. ICOTOM 5* (edited by G. Gottstein and K. Lücke), p. 265. Springer Verlag, New York (1978).
47. H. Honneff and H. Mecking, *Proc. 6th Int. Conf. on Tex. of Mat. ICOTOM 6* (edited by S. Nagashima), p. 347. Iron and Steel Inst. of Japan (1981).

48. J. L. Raphanel and P. van Houtte, *Acta metall.* **33**, 1481 (1985).
49. M. Renouard and M. Wintenberger, *C. r. Acad. Sci.* **B283**, 237 (1967).
50. D. Raabe and K. Lücke, *Mater. Sci. Technol.* **9**, 302 (1993).
51. D. Raabe and K. Lücke, *Proc. 10th Int. Conf. on Tex. of Mat. ICOTOM 10, Materials Science Forum* **157-162**, 1469 (1994).
52. E. Aernoudt, P. van Houtte and T. Leffers, In *Materials Science and Technology* (edited by R. W. Cahn, P. Haasen and E. J. Kramer), Vol. 6, p. 86. VCH (1993).
53. L. G. Schulz, *J. appl. Phys.* **20**, 1030 (1949).
54. H. J. Bunge and C. Esling, *J. Phys. Lett.* **40**, 627 (1979).
55. M. Dahms and H. J. Bunge, *J. appl. Cryst.* **22**, 439 (1989).
56. M. Dahms, *Text. Microstr.* **19**, 169 (1992).
57. E. Sachs, *Z. Verein Deutsch. Ingen.* **72**, 734 (1928).
58. P. Wagner, Ph.D. Thesis, RWTH, Aachen (1994).
59. T.-T. Wang, B. L. Adams and P. R. Morris, *Metall. Trans A* **21A**, 2223 (1990).
60. C. S. Lee, D. J. Duggan and R. E. Smallman, *Acta metall.* **41**, 2265 (1993).
61. M. F. Ashby, *Phil. Mag.* **21**, 399 (1970).
62. O. Engler and G. Gottstein, *Steel Res.* **63**, 413 (1992).
63. J. Venables and C. Harland, *Phil. Mag.* **27**, 1193 (1973).